

Local structural distortions drive magnetic molecular field in a compositionally complex spinel oxide

Rukma Nevgi,^{1,*} Subha Dey,^{1,†} Nandana Bhattacharya,¹ Tinku Dan,² Sujay Chakravarty,³
S. D. Kaushik,⁴ Christoph Klewe,⁵ George E. Sterbinsky,⁶ and Srimanta Middey^{1,‡}

¹*Department of Physics, Indian Institute of Science, Bengaluru 560012, India*

²*Deutsches Elektronen-Synchrotron DESY, 22607 Hamburg, Germany*

³*UGC-DAE CSR Kalpakkam Node Kokilamedu-603104, Tamilnadu, India*

⁴*UGC-DAE Consortium for Scientific Research Mumbai Centre,
R5 Shed, Bhabha Atomic Research Centre, Mumbai 400085, India*

⁵*Advanced Light Source, Lawrence Berkeley National
Laboratory, Berkeley, California 94720, USA*

⁶*Advanced Photon Source, Argonne National Laboratory, Lemont, Illinois 60439, USA*

Abstract

A core challenge in understanding high entropy oxides (HEOs) is how these systems, with five or more cations at a crystallographic site, can withstand local distortions while preserving a uniform structure on a larger scale. We address this for spinel HEO by comparatively examining extended X-ray absorption fine structure (EXAFS) on $(\text{Mn}_{0.2}\text{Co}_{0.2}\text{Ni}_{0.2}\text{Cu}_{0.2}\text{Zn}_{0.2})\text{Cr}_2\text{O}_4$ ($A^5\text{Cr}_2\text{O}_4$) and its parent counterparts $A\text{Cr}_2\text{O}_4$ ($A = \text{Mn}, \text{Co}, \text{Ni}, \text{Cu}, \text{Zn}$). Unlike the HEO with rock-salt structure, the element-specific distortions in disordered sublattice go beyond the first neighbor here. Moreover, the tetragonal distortion around the Cu^{2+} ion, known as a textbook example of the Jahn-Teller effect, is highly reduced in $A^5\text{Cr}_2\text{O}_4$ compared to CuCr_2O_4 . Despite variations in the A-O bond lengths, the inter-cationic distances remained remarkably similar. This affirms a high level of flexibility in the positioning of oxygen, enabling them to adapt to the overall cubic symmetry. Despite containing multiple magnetic ions, the Curie-Weiss temperature and effective magnetic moments of $A^5\text{Cr}_2\text{O}_4$ are similar to those of NiCr_2O_4 . This can be attributed to both materials' comparable local bond lengths around Cr, as evidenced by EXAFS analysis. This study conclusively presents a method for elucidating how local structural distortions influence the macroscopic properties of compositionally complex quantum materials.

The periodic arrangement of atoms/ions/molecules within crystalline materials is the backbone of their diverse electronic, magnetic, and topological properties. Conventionally, crystalline materials are synthesized based on the principle of enthalpy minimization. However, in recent years, there has been a surge of interest in high-entropy materials that break this paradigm, where high configurational entropy drives structure formation [1–7]. Originally introduced for multicomponent alloys [8, 9], this concept was extended to oxide ceramics in 2015 by demonstrating the stabilization of $\text{Mg}_{0.2}\text{Co}_{0.2}\text{Ni}_{0.2}\text{Cu}_{0.2}\text{Zn}_{0.2}\text{O}$ in a rock-salt structure [10]. Since then, high entropy oxides (HEOs) have been synthesized with a variety of structures, such as fluorites ($\text{AO}_{2-\delta}$) [11], perovskites (ABO_3) [12–15], spinels (AB_2O_4) [16–18], and pyrochlores ($\text{A}_2\text{B}_2\text{O}_7$) [19–21], where at least one of the crystallographic sites is occupied by five or more elements in equal or nearly equal atomic fractions. Despite not all being entropy-stabilized [5], these compositionally complex oxides (CCOs) exhibit interesting properties beyond their single element counterparts and hold potential for applications such as energy storage, catalysis, and microwave absorption [22–28].

Deciphering the interplay among disorder, distortions, and electronic/magnetic properties within a CCO is a major hurdle [29]. In conventional oxides with low disorder, distortions around individual cations are generally related to their ionic radii, coordination numbers, and oxidation states, which control electron hopping and magnetic exchange interaction strength. The local distortions around each cation within the disordered sublattice of CCO are expected to be highly variable and likely to deviate significantly from the average long-range structure probed by the diffraction technique. It is also necessary to determine the extent of this local distortion variation across neighboring elements and how it affects the material’s properties. To address these issues, we employ the extended X-ray absorption fine structure (EXAFS) technique, which is an element-specific method used to study the local chemical distribution (length scale $\sim 1\text{-}10$ Å) around particular atoms [30–32]. EXAFS spectra are specifically sensitive to the coordination number, bond distances, and atomic species surrounding the core atom, providing a relatively simple way to understand the local structural distortion. Interestingly, EXAFS studies have shown that the variation in cation-specific bond lengths is confined only to the first coordination shell in the case of rock-salt HEOs [33, 34]. This work focuses on how spinel oxide handles local distortions and how these influence the magnetic interaction energies.

The normal AB_2O_4 spinel consists of a diamond lattice formed by the tetrahedrally coordinated A site and a pyrochlore lattice formed by the octahedrally coordinated B site [Fig.

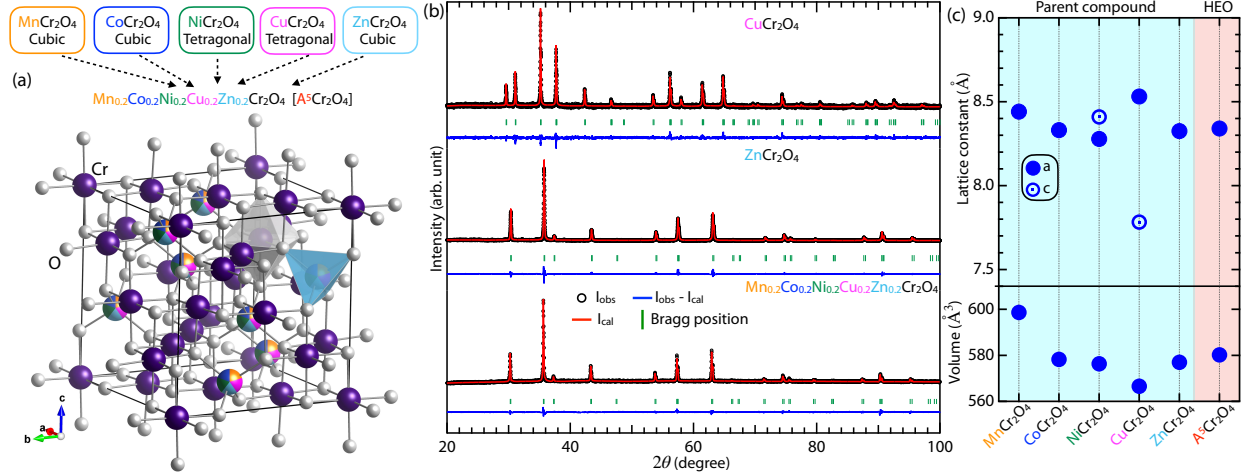


FIG. 1. **Structural characterization using X-ray diffraction.** **a** Schematic of $A^5\text{Cr}_2\text{O}_4$ with cubic spinel structure having Cr at the octahedral site and A ($= \text{Mn, Co, Ni, Cu}$ and Zn) at the tetrahedral site. **b** Rietveld refined XRD data for CuCr_2O_4 and ZnCr_2O_4 along with $A^5\text{Cr}_2\text{O}_4$. **c** The lattice parameters for the parent compounds and $A^5\text{Cr}_2\text{O}_4$ as obtained from the Rietveld analysis. The parameter a in the tetragonal phases of NiCr_2O_4 and CuCr_2O_4 have been multiplied by $\sqrt{2}$ for ease of comparison.

1(a)]. The spinel family has been extensively studied for over a century due to the observation of various phenomena, such as magnetic ordering, frustrated magnetism, orbital ordering, charge ordering, metal-insulator transitions, etc [35]. We focused on the $A\text{Cr}_2\text{O}_4$ family of compounds with normal spinel structures and successfully synthesized a new compound: $(\text{Mn}_{0.2}\text{Co}_{0.2}\text{Ni}_{0.2}\text{Cu}_{0.2}\text{Zn}_{0.2})\text{Cr}_2\text{O}_4$ (hereafter referred to as $A^5\text{Cr}_2\text{O}_4$). The individual members MnCr_2O_4 and CoCr_2O_4 are cubic and become ferrimagnetic at T_c values of 41 K and 93 K, respectively [36–39]. Additionally, they exhibit multiferroic behavior below 18 K and 27 K [36–39]. Due to the Jahn-Teller activity of the Ni^{2+} and Cu^{2+} ions, NiCr_2O_4 and CuCr_2O_4 undergo cubic to tetragonal transitions below 310 K and 853 K, respectively. They transform into an orthorhombic phase at 65 K and 125 K, respectively, accompanied by a ferrimagnetic transition [40]. On the other hand, ZnCr_2O_4 is cubic at room temperature and exhibits an antiferromagnetic ordering transition below 12 K [41].

In the present work, we probed the modification of the local structure of $A^5\text{Cr}_2\text{O}_4$ compared to that of its five undoped counterparts ($A\text{Cr}_2\text{O}_4$, $A = \text{Mn, Co, Ni, Cu, Zn}$) at room temperature. X-ray diffraction (XRD) and X-ray absorption spectroscopy (XAS) of the transition metal $L_{3,2}$ edges confirmed the desired normal spinel structure of $A^5\text{Cr}_2\text{O}_4$ with cubic symmetry. Our comprehen-

sive EXAFS measurements revealed a high degree of similarity between the local environment surrounding Cr in $A^5\text{Cr}_2\text{O}_4$ and that surrounding Cr in pristine CoCr_2O_4 , ZnCr_2O_4 , and NiCr_2O_4 . However, the local structural distortions around the individual A -sites of $A^5\text{Cr}_2\text{O}_4$ differ from each other and persist beyond the first neighbor. Interestingly, the Jahn-Teller distortions typically observed in the CuCr_2O_4 are significantly suppressed in $A^5\text{Cr}_2\text{O}_4$, which is compensated for by a reduction in the length of the bonds surrounding the Mn. Moreover, the oxygen atoms in $A^5\text{Cr}_2\text{O}_4$ are rearranged relative to their original positions in the parent compounds to accommodate the variations in local distortions. This enables $A^5\text{Cr}_2\text{O}_4$ to maintain its overall cubic structure. We found that the magnetic response of $A^5\text{Cr}_2\text{O}_4$ is contributed by all magnetic ions: Cr^{3+} and A^{2+} ($A = \text{Mn}, \text{Co}, \text{Ni}$ and Cu). Finally, EXAFS and Curie-Weiss analysis of the magnetic data establish a direct correlation between the mean-field magnetic interaction energy scale and the Cr-O and Cr-Cr bond lengths.

Results:

Synthesis and crystal structure: The synthesis of polycrystalline samples of five parent compounds $A\text{Cr}_2\text{O}_4$ ($A = \text{Mn}, \text{Co}, \text{Ni}, \text{Cu}$ and Zn) and $A^5\text{Cr}_2\text{O}_4$ was carried out using a conventional solid-state synthesis route (details are provided in the Methods section). The powder X-ray diffraction (XRD) pattern of $A^5\text{Cr}_2\text{O}_4$ at room temperature is compared with that of two parent members, tetragonal CuCr_2O_4 and cubic ZnCr_2O_4 , in Fig. 1(b). Similar to ZnCr_2O_4 , the diffraction pattern of $A^5\text{Cr}_2\text{O}_4$ can be indexed and refined with a normal spinel structure with cubic symmetry having a space group of $Fd\bar{3}m$ (space group number: 227). The diffraction patterns and structural information obtained from the refinement of all six compounds are shown in the Supplementary Information (Table S1 and Fig. S1). The lattice constants and lattice volumes for the five parent members and $A^5\text{Cr}_2\text{O}_4$ at room temperature are shown in Fig. 1(c). For comparison, the lattice constant a of the tetragonal members NiCr_2O_4 and CuCr_2O_4 is multiplied by $\sqrt{2}$ (see Supplementary Fig. S2). The trend in lattice parameters and volume can be understood by considering the ionic radii of A^{2+} ions. The average ionic radii (0.592 Å) of the A -site for $A^5\text{Cr}_2\text{O}_4$ are closer to those of Zn^{2+} (0.60 Å) and Co^{2+} (0.58 Å) [ionic radii of Mn^{2+} : 0.66 Å, Ni^{2+} : 0.55 Å, and Cu^{2+} : 0.57 Å] [44], leading to similar unit cell volumes of $A^5\text{Cr}_2\text{O}_4$ and $A\text{Cr}_2\text{O}_4$ ($A = \text{Co}$ and Zn). Although NiCr_2O_4 is tetragonal, the Jahn-Teller distortion is very small at 300 K, and the unit cell volume is very similar. It can also be inferred from Fig. 1(c) that the Mn and Cu ions are likely to experience internal stress (compressive for Mn and tensile for Cu) when introduced into $A^5\text{Cr}_2\text{O}_4$, leading to strong local distortions.

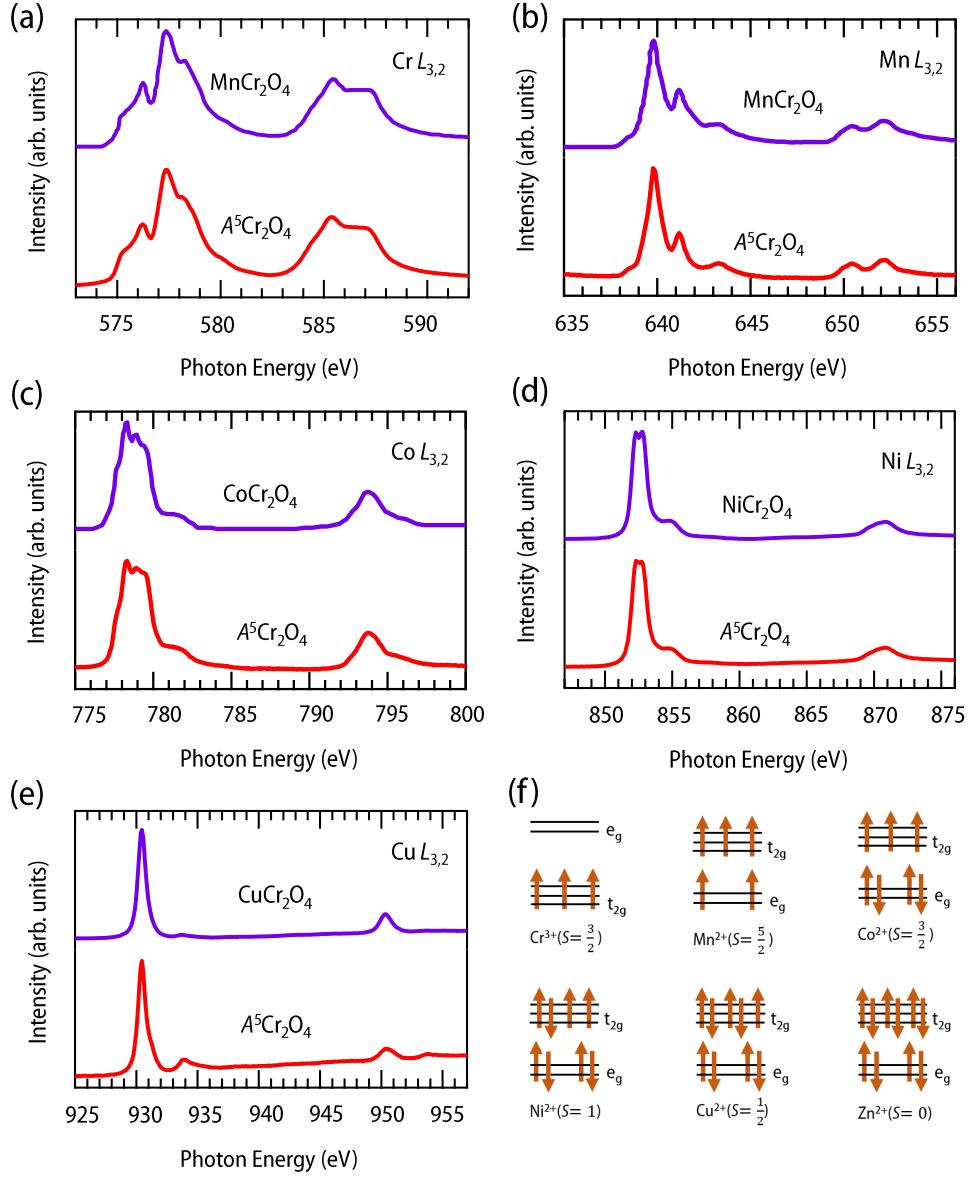


FIG. 2. **Determination of oxidation state using X-ray absorption spectroscopy.** **a** Cr $L_{3,2}$ edge in $MnCr_2O_4$ and $A^5Cr_2O_4$. **b** Mn $L_{3,2}$ edge in $MnCr_2O_4$ and $A^5Cr_2O_4$. **c** Co $L_{3,2}$ edge in $CoCr_2O_4$ and $A^5Cr_2O_4$. **d** Ni $L_{3,2}$ edge in $NiCr_2O_4$ and $A^5Cr_2O_4$. **e** Cu $L_{3,2}$ edge in $CuCr_2O_4$ and $A^5Cr_2O_4$. The spectra of Cr and Mn for $MnCr_2O_4$ is taken from Ref. 42. The spectra of Co for $CoCr_2O_4$ is adapted from Ref. 43. **f** Spin configurations of Cr, Mn, Co, Ni, Cu, and Zn cations in $A^5Cr_2O_4$. The energy gap between t_{2g} and e_g is not according to the scale.

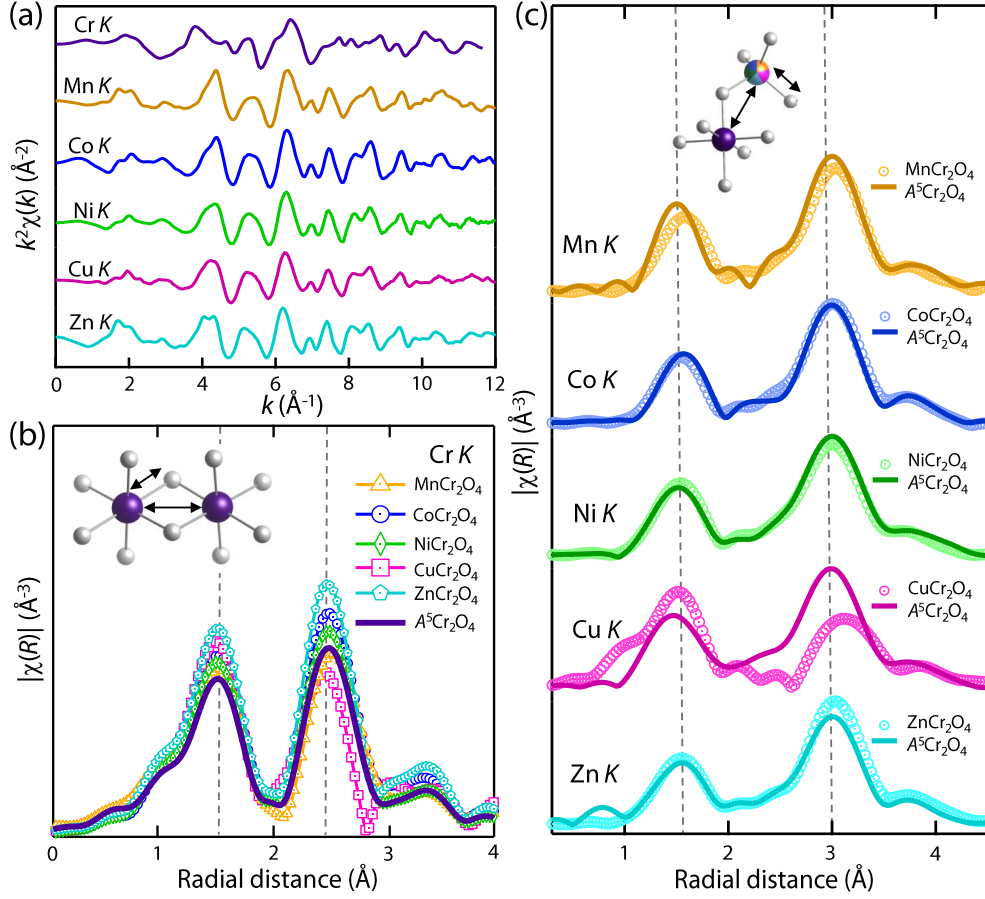


FIG. 3. **Probing the local structure using EXAFS.** **a** The k weighted EXAFS spectra in $A^5Cr_2O_4$. The Fourier transform of the EXAFS spectra at **b** Cr K -edge and **c** A K -edges in the parent oxides and $A^5Cr_2O_4$. The first and second nearest neighbor distances have also been shown as an inset of panels b and c.

Transition metal valency and crystal field environment: In all parent ACr_2O_4 compounds, the cations A^{2+} occupy the tetrahedral site, while Cr^{3+} occupies the octahedral site [35]. To explore the same phenomenon in $A^5Cr_2O_4$, we carried out element-specific XAS experiments on the $L_{3,2}$ edges of transition metal ions because the XAS spectral line shape for the $2p^63d^n \rightarrow 2p^53d^{n+1}$ transition is strongly dependent on the valency, spin character of the initial state and crystal field environment of the system [45]. The XAS spectra for the $L_{3,2}$ edges of Cr, Mn, Co, Ni, and Cu in $A^5Cr_2O_4$, recorded in total electron yield mode, were compared with those of the corresponding parent compounds, as shown in Fig. 2 (a)-(e). It is evident that the spectra of Cr, Mn, Co, and Ni for $A^5Cr_2O_4$ look exactly similar to the corresponding edges of the parent compounds [42, 43, 46]. Although the main features of Cu $L_{3,2}$ XAS for $A^5Cr_2O_4$ are quite similar to those of the parent

CuCr_2O_4 , the features at approximately 933.9 eV and 953.7 eV are more intense. This slight difference may be attributed to the reduced Jahn-Teller distortion in $A^5\text{Cr}_2\text{O}_4$ (demonstrated in the latter part of the manuscript). Overall, our XAS measurements further established a normal spinel structure similar to that of all the parent compounds. Fig. 2(f) shows the expected spin configurations for each of the cations of $A^5\text{Cr}_2\text{O}_4$, according to the oxidation state found by XAS. This is further corroborated by the Curie–Weiss analysis of magnetic susceptibility, which is demonstrated in the latter part of the manuscript.

Element specific local distortions using EXAFS: To investigate the local structural distortions around Cr, Mn, Co, Ni, Cu, and Zn, we recorded the K -edge EXAFS spectra. The spectra of every transition metal edge were calibrated using the corresponding standard metal foils. To avoid interference from the next absorption edge in $A^5\text{Cr}_2\text{O}_4$, the spectra were truncated above 12 \AA^{-1} in k space. Similar features across Mn, Co, Ni, Cu, and Zn K -edges [Fig. 3(a)] suggest a similar coordination geometry with a uniform distribution throughout the lattice. The Fourier transform (FT) of $k^2 \cdot \chi(k)$ of Cr and A K -edges for each of the parent compounds and $A^5\text{Cr}_2\text{O}_4$ are shown in Fig. 3(b) and (c), respectively. The first peak at 1.55 \AA in both Cr and A K -edge data suggests similar Cr-O and A -O distances in parent compounds. The second peak at 2.5 \AA in Cr K -edge data corresponds to Cr-Cr distance, while the one at 3 \AA in A K -edge data corresponds to A -Cr distance, implying different cation environments. We also note that the real scattering distance shifts by approximately 0.5 \AA as the phase shift in the Fourier transform remains uncorrected.

The FT of $k^2 \cdot \chi(k)$ for Cr K in $A^5\text{Cr}_2\text{O}_4$ [Fig. 3(b)] shows similar features like the parent compounds (except CuCr_2O_4). However, Fig. 3(c) reveals significant changes in local structures around Cu and Mn in $A^5\text{Cr}_2\text{O}_4$ compared to CuCr_2O_4 and MnCr_2O_4 , respectively. This is likely due to the difference in crystal symmetry (cubic vs. tetragonal) and lattice volume changes. Local structures around Co, Ni, and Zn in $A^5\text{Cr}_2\text{O}_4$ are similar to their parent compounds, except for a slight change in Zn-Cr distance. These spectra clearly demonstrate that the local distortions vary across the A -sites, extending beyond the first neighbor in $A^5\text{Cr}_2\text{O}_4$.

To quantify the effect of all differences shown in Fig. 3, we performed fittings for the A K -edge spectra ($A = \text{Mn, Co, Ni, Cu and Zn}$) in every parent compound in the k range of 2 to 14 \AA^{-1} and the R range of 1 to 4.5 \AA (details are in the Methods section). For the Cr K -edge, the k range of 2 to 12 \AA^{-1} and the R range of 1 to 3.7 \AA were employed in fittings. The analysis considered structural symmetries determined by XRD. The best fits obtained for the Cr local structure in cubic ZnCr_2O_4 , $A^5\text{Cr}_2\text{O}_4$ and tetragonal CuCr_2O_4 are depicted in Fig. 4 (a)-(c). In the cubic model, a Cr

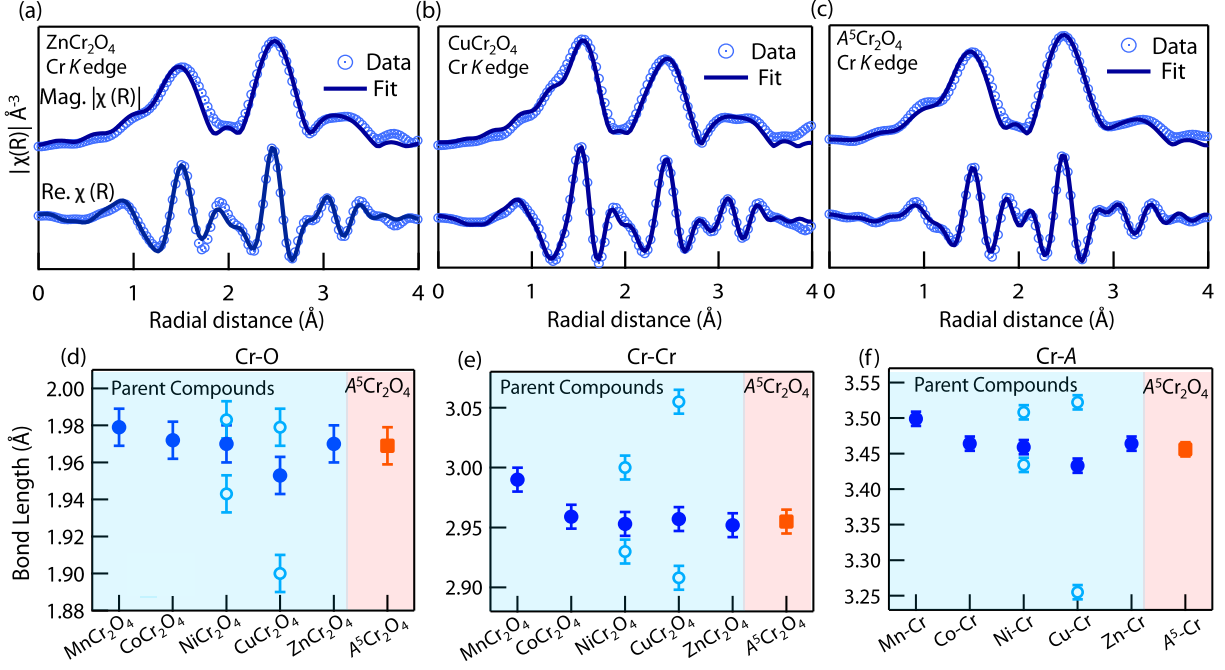


FIG. 4. Analysis of local structure in the octahedral environment. The Fourier transformed EXAFS spectra along with the fitted data [the magnitude $|\chi(R)|$ and the real part $\text{Re. } \chi(R)$] in **a** ZnCr_2O_4 , **b** CuCr_2O_4 and **c** $A^5\text{Cr}_2\text{O}_4$. The distance between **d** Cr and the first neighbor O, **e** Cr and the second neighbor Cr, **f** Cr and the third neighbor *A* cations in pristine chromite spinels and $A^5\text{Cr}_2\text{O}_4$. Due to Jahn-Teller distortion, NiCr_2O_4 and CuCr_2O_4 display two bond lengths (drawn as open circles), whose weighted average (denoted by the closed circle) is also plotted for ease of comparison.

cation has 6 O anions as first neighbors (Fig. 4 (d)), 6 Cr cations as second neighbors (Fig. 4 (e)), and 6 *A* cations as third neighbors (Fig. 4 (f)). In the tetragonal model, six equal bond lengths in each case split into equal bond distances with coordination four and two, whose weighted average is plotted (denoted by closed circles) for easier comparison (for NiCr_2O_4 and CuCr_2O_4). From the analysis, we could infer that the bond distances Cr-O (1.97 Å), Cr-Cr (2.96 Å) and Cr-*A* (3.46 Å) in $A^5\text{Cr}_2\text{O}_4$ are akin to that of CoCr_2O_4 , ZnCr_2O_4 and also with the weighted average bond lengths of NiCr_2O_4 . Consistent with the difference in lattice constant, these bond lengths are higher in MnCr_2O_4 . Also, the average Cr-O and Cr-*A* bond distances of CuCr_2O_4 are lower compared to $A^5\text{Cr}_2\text{O}_4$.

Cr EXAFS, averaging local Cr environments, can't distinguish distortions caused by specific *A* cations (*e.g.* Mn vs Cu). Analyzing *A*-site EXAFS in $A^5\text{Cr}_2\text{O}_4$ versus $A\text{Cr}_2\text{O}_4$ reveals these

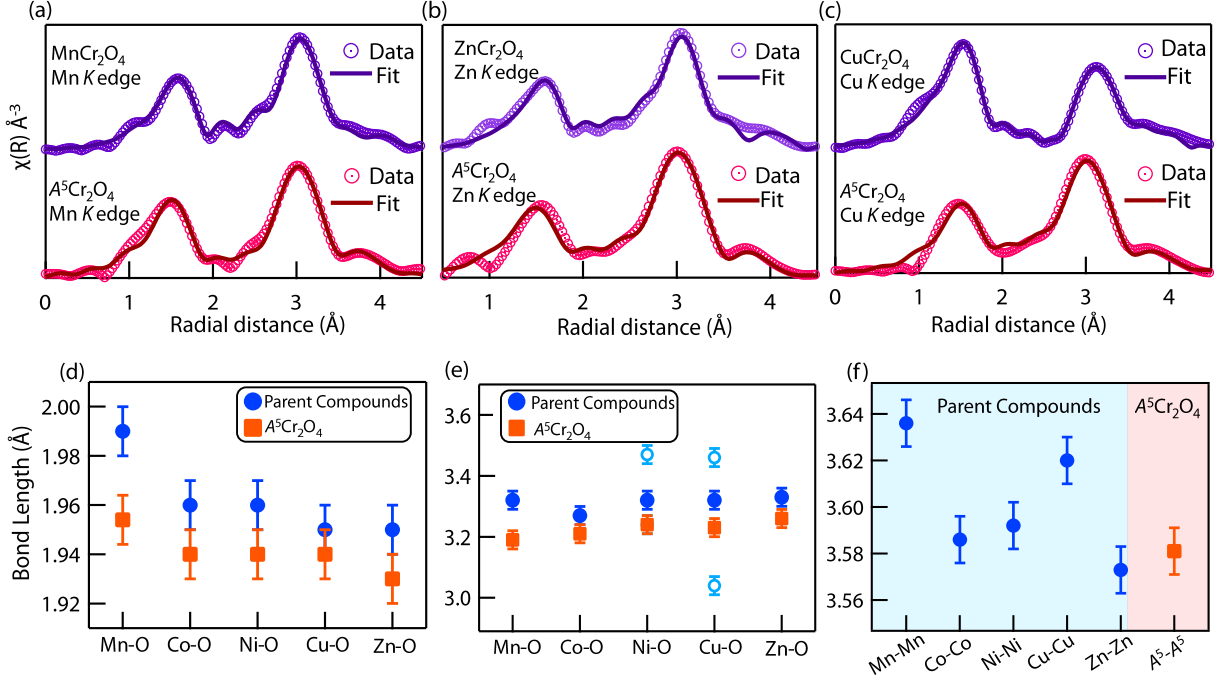


FIG. 5. Analysis of local structure in the tetrahedral environment. The magnitude of the Fourier transformed EXAFS spectra along with fitting obtained at the **a** Mn *K*-edge in MnCr_2O_4 and $A^5\text{Cr}_2\text{O}_4$, **b** Zn *K*-edge in ZnCr_2O_4 and $A^5\text{Cr}_2\text{O}_4$ and **c** Cu *K*-edge in CuCr_2O_4 and $A^5\text{Cr}_2\text{O}_4$. A comparison of bond distances between **d** the *A* cations and the first neighbor O, **e** the *A* cations and the second neighbor O, **f** two *A* cations in the pristine chromite oxides and $A^5\text{Cr}_2\text{O}_4$. In **e**, due to Jahn-Teller distortion, NiCr_2O_4 , and CuCr_2O_4 display two bond lengths between *A* cations and O anions (drawn as open circles), whose weighted average (closed cycle) is plotted for ease of comparison. As one of the second neighbor Ni-O bond length $\sim 3.23 \text{ \AA}$ of NiCr_2O_4 is the same as in $A^5\text{Cr}_2\text{O}_4$, no distinction can be made between the two values in panel **e**.

element-specific distortions [see Fig. 5 (a-c), Fig. S3 and Supplementary Tables S2, S3, and S4]. Interestingly, *A* ions share the same coordination for first-neighbor oxygen and fourth-neighbor *A* cation for both cubic and tetragonal structures. In case of cubic MnCr_2O_4 , we find that Mn has 4 O at $R = 1.99 \text{ \AA}$, 12 O at $R = 3.32 \text{ \AA}$, 12 Cr at $R = 3.50 \text{ \AA}$ and 4 Mn as at $R = 3.64 \text{ \AA}$ as direct scatterers. The Cr-Mn distance obtained from the Cr *K*-edge EXAFS analysis and the Mn-Cr distance obtained from Mn *K*-edge EXAFS fitting were very similar. In the case of tetragonal CuCr_2O_4 , the analysis of Cu *K*-edge finds 4 O at $R = 1.95 \text{ \AA}$, 8 O at $R = 3.46 \text{ \AA}$ and 4 O at $R = 3.04 \text{ \AA}$, 8 Cr at $R = 3.52 \text{ \AA}$ and 4 Cr at $R = 3.26 \text{ \AA}$, and 4 Cu at $R = 3.61 \text{ \AA}$ as direct scatterers.

The EXAFS fittings of each A -site of $A^5\text{Cr}_2\text{O}_4$ were performed considering cubic symmetry in accordance with the XRD result. Excellent fitting has been found for each case, including Cu K -edge [Fig. 5 (c)] and Ni K -edge (see Supplementary Fig. S3 (c)). We have also attempted to fit Cu K EXAFS of $A^5\text{Cr}_2\text{O}_4$ using tetragonal symmetry, similar to the parent compound CuCr_2O_4 . However, such fitting results in negative σ^2 (see Supplementary Table S5) for Cu. This exclusively demonstrates that even the local Jahn-Teller distortion is either fully absent or highly suppressed in $A^5\text{Cr}_2\text{O}_4$. This contrasts sharply with Cu-containing rock-salt HEO, where the Cu can maintain clear Jahn-Teller distortions locally [33, 47].

The comparison of each neighbor distance among the pristine members and doped compound reveals several interesting trends (Fig. 5 (d)-(f)). The Mn-O distance in MnCr_2O_4 is the largest due to its bigger unit cell volume than other pristine materials. In $A^5\text{Cr}_2\text{O}_4$, the first neighbor A -O distance depends on the specific element positioned at the A -site. The Co-O, Ni-O, and Cu-O distances are very similar, whereas Mn-O and Zn-O distances differ. Notably, the A -O bond distances are smaller than those in parent $A\text{Cr}_2\text{O}_4$, indicating that these local variations are not simply due to changes in the overall crystal volume. Importantly, this study has revealed a strong variation in second neighbor A -O distances in disordered $A^5\text{Cr}_2\text{O}_4$, suggesting that local structural distortions extend beyond the first-neighbor shell. Interestingly, the second-neighbor Mn-O bond length (Fig. 5(e)) is the shortest among all A -O distances in $A^5\text{Cr}_2\text{O}_4$, which is in stark contrast to its longest first-neighbor distance (Fig. 5(d)). This strongly suggests that the oxygen sublattice can adjust to accommodate the variations caused by different A -site cations. The fourth neighbor A - A distance is found to be $\simeq 3.58 \pm 0.02 \text{ \AA}$ in the fittings of each A -site EXAFS. (See Supplementary Tables S2, S3 and S4). This A - A bond length is comparable to those in CoCr_2O_4 , NiCr_2O_4 , and ZnCr_2O_4 , but smaller to the ones in MnCr_2O_4 , and CuCr_2O_4 . The EXAFS analysis suggests that all cation-cation distances in $A^5\text{Cr}_2\text{O}_4$ are similar, implying that all A cations form a uniform diamond sublattice. Consequently, the oxygen anions shift from their ideal positions to accommodate these local distortions, resulting in varying A -O bond lengths.

Correlation between structural distortions and magnetic interaction: The bond lengths derived from EXAFS analysis are expected to play a crucial role in comprehending the strength of magnetic interactions in $A\text{Cr}_2\text{O}_4$ spinels. The theory of ground state magnetic configuration of cubic $AB_2\text{O}_4$ is very often described by the following Hamiltonian with classical Heisenberg spins considering B - B , and A - B exchanges, initially proposed by Lyons, Kaplan, Dwight, and Menyuk [35, 48, 49].

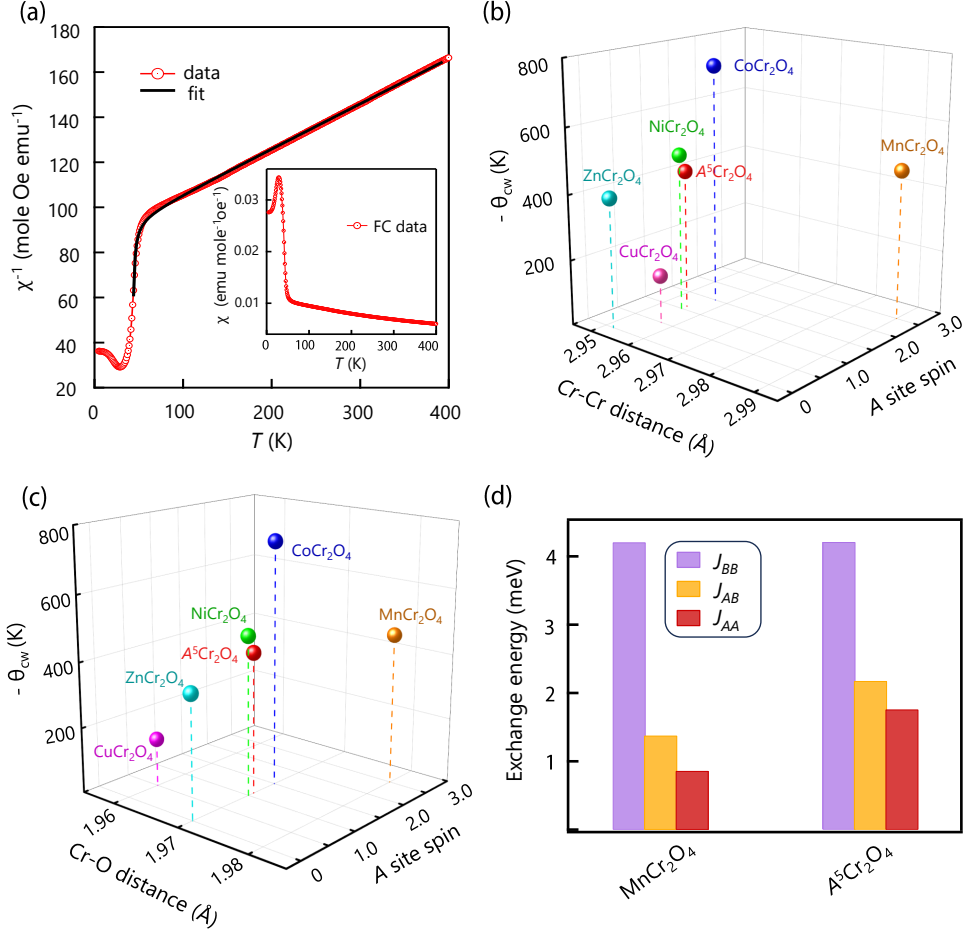


FIG. 6. **Magnetic characterization and its connection with local structure** **a** Fitting of inverse magnetic dc susceptibility using Curie-Weiss equation above T_N in $A^5Cr_2O_4$ at 5000 Oe. Inset features field cooled (FC) dc susceptibility as a function of temperature. $-\theta_{CW}$ is plotted as a function of **b** Cr-Cr bond distance and *A*-site spin and **c** Cr-O bond distance and *A* site spin in parent oxides and $A^5Cr_2O_4$. **d** A comparison of the magnetic exchange interaction energy between two Cr cations (J_{BB}), between Cr and *A* (J_{AB}), and between two *A* cations (J_{AA}) in $MnCr_2O_4$ and $A^5Cr_2O_4$.

$$H = 2J_{AB}S_A S_B \left(\sum_{\langle ij \rangle} \vec{\sigma}_i^A \cdot \vec{\sigma}_j^B + \frac{3u}{4} \sum_{\langle ij \rangle} \vec{\sigma}_i^B \cdot \vec{\sigma}_j^B \right) \quad (1)$$

The sums are over nearest-neighbor *A*-*B* and *B*-*B* pairs and the parameter $u = \frac{4J_{BB}S_B}{3J_{AB}S_A}$ and $\vec{\sigma}_j^\alpha = \vec{S}_j^\alpha / S_j^\alpha$ with $\alpha=A$ and *B*. The interaction within the diamond sublattice (J_{AA}) has also been claimed to be important in recent studies [50, 51]. In chromite spinels, the magnetic interaction

between two Cr is a direct exchange and thus depends strongly on the Cr-Cr distance [50]. The superexchange between A and Cr is mediated through interconnecting oxygen, and the strength will depend on the bond lengths A -O and Cr-O, A -O-Cr bond angle and the electronic configuration of A ions. Due to the presence of multiple magnetic ions at A -site with different A -O bond lengths leading to a varying strength of J_{AB} and J_{AA} , the microscopic description of spin arrangements is expected to be complex in $A^5\text{Cr}_2\text{O}_4$ and requires a separate detailed study. Interestingly, a direct dependence of magnetic transition temperatures on the average crystal structure of perovskite HEOs has been demonstrated, even though the details of the magnetic features within the magnetically ordered phase is more complicated [52–56]. In the case of parent $A\text{Cr}_2\text{O}_4$ members, the magnetic frustration caused by antiferromagnetic Cr-Cr interactions within the pyrochlore sublattice varies, resulting in a very reduced magnetic ordering temperature compared to the Curie-Weiss temperature (θ_{CW}) (Supplementary Table S5). As θ_{CW} is a measure of molecular field and considered as an approximate indicator of the strength of mean-field magnetic interaction between the ions [57], we have focused on finding out any relation between θ_{CW} and the bond lengths at 300 K obtained from the EXAFS analysis.

The temperature-dependent magnetic susceptibility [$\chi=M/H$] for $A^5\text{Cr}_2\text{O}_4$, measured under a magnetic field (H) of 5000 Oe in field cooled condition has been depicted as an inset of Fig. 6 (a). We found a magnetic transition around 50 K. The main panel represents the fitting of the inverse of dc susceptibility at high temperature using molecular field theory of a ferrimagnet [58]

$$\chi^{-1} = \frac{T - \theta_{\text{CW}}}{C_A + 2C_B} - \frac{C''}{T - \theta'} \quad (2)$$

The first term is the hyperbolic high-temperature linear part with a Curie-Weiss form, where C_A and C_B correspond to Curie constants related to the two magnetic sublattices M_A and M_B , respectively. θ_{CW} is the Curie-Weiss temperature. The second term is the hyperbolic low- T asymptote, where C'' and θ' are constants akin to different Weiss coefficients that represent the inter and intrasublattice interactions. From this fitting, we have obtained a Curie-Weiss temperature of $\theta_{\text{CW}} = -432$ K and the effective magnetic moment of $6.33 \mu_B/\text{f.u.}$ using the formula $\mu_{\text{eff}} = \sqrt{\frac{3K_B(C_A+2C_B)}{N_A}}$ [59], where K_B is Boltzmann's constant and N_A is Avogadro's number. Interestingly, μ_{eff} is very similar to the expected value of $6.26 \mu_B/\text{f.u.}$, calculated by considering the average magnetic moments of A^{2+} ($A = \text{Mn, Co, Ni, Cu}$; Zn^{2+} is nonmagnetic) and Cr^{3+} of $A^5\text{Cr}_2\text{O}_4$ ($\mu_{\text{eff}} = \sqrt{2\mu_{\text{Cr}}^2 + \mu_A^2}$). The most surprising finding is that despite having a series of magnetic interactions [Cr- A and A - A' with $A, A' = \text{Mn, Co, Ni, Cu}$], the θ_{CW} of $A^5\text{Cr}_2\text{O}_4$ is com-

parable to NiCr_2O_4 [40] (also see Supplementary Figure S4) and MnCr_2O_4 [50]. The effective magnetic moment also closely resembles NiCr_2O_4 ($6.64 \mu_B/\text{f.u.}$). These findings also indicate that the net magnetic interaction, felt by a magnetic ion in CCO, can be treated using a mean-field approach.

To understand the effect of local distortions on magnetism, $|\theta_{\text{CW}}|$ for all six compounds have been plotted as a function of EXAFS derived bond lengths and the A -site spin value in Fig. 6(b), (c). The θ_{CW} of the parent compounds $A\text{Cr}_2\text{O}_4$ is obtained from Ref. [40, 50, 60] and an average of A -site spin ($S_A=1.1$) for $A^5\text{Cr}_2\text{O}_4$ has been considered for these plots. The Cr-Cr bond length (Fig.6 (b)) is considered as it corresponds to the Cr-Cr direct exchange. The Cr-O bond length is also plotted in connection with the A -O-Cr superexchange path (Fig.6 (b)). While the A -O bond length also plays a role in A -O-Cr superexchange strength, we were unable to create a similar plot for A -O bond lengths because this distance depends on the specific atom occupying the A -site in $A^5\text{Cr}_2\text{O}_4$. The θ_{CW} of $A^5\text{Cr}_2\text{O}_4$ is closer to the value of NiCr_2O_4 and MnCr_2O_4 . We have further evaluated the mean-field magnetic exchange parameters from our magnetization data, following the process described in Ref. [50] [also see Supplementary]. The exchange interaction parameters J_{BB} (interactions between two Cr^{3+}), J_{AB} (between A^{2+} and Cr^{3+}), and J_{AA} (between two A^{2+} cations) have been compared in Fig. 6(d). The exchange parameters for MnCr_2O_4 have been adapted from Ref. [50]. Interestingly, the J_{BB} interaction shows almost no difference between these compounds. However, the J_{AB} and J_{AA} values for $A^5\text{Cr}_2\text{O}_4$ higher than those of MnCr_2O_4 . The extraction of these J s using equation 2 is not possible for NiCr_2O_4 due to an anomaly in the magnetic susceptibility at the cubic-to-tetragonal transition (~ 315 K, see Supplementary Fig S4). However, Fig.6 (b) and (c) clearly demonstrate the close similarity between $A^5\text{Cr}_2\text{O}_4$ and NiCr_2O_4 in terms of key parameters like Cr-Cr distance, Cr-O distance, and A -site spin and θ_{CW} . This strong resemblance highlights the crucial role of local bond lengths around the Cr ions in determining the mean-field magnetic interactions within $A^5\text{Cr}_2\text{O}_4$.

Discussions: We have synthesized a new compositionally complex oxide $A^5\text{Cr}_2\text{O}_4$ having a normal spinel structure, with Cr^{3+} ions occupying the octahedral site and a uniform distribution of A^{2+} ($A = \text{Mn}, \text{Co}, \text{Ni}, \text{Cu}, \text{and Zn}$) ions in the tetrahedral site. Employing element-specific EXAFS analysis, our investigation of the local structure reveals several unique features that distinguish it from previously reported high entropy oxides. Unlike HEOs with rock-salt structures [33, 47], where local Jahn-Teller distortions around Cu^{2+} ions are typically preserved, our study reveals a significant reduction or even a complete absence (within the resolution power of EXAFS) of such

distortions in $A^5\text{Cr}_2\text{O}_4$. In contrast to previous EXAFS studies of rock-salt HEOs [33, 34], where distortions around A^{2+} cations were limited to the first nearest neighbors and second-neighbor distances remained uniform, $A^5\text{Cr}_2\text{O}_4$ exhibits variation in local distortions extending beyond the first neighbors. Despite variation in A -O bond distances, A - A distances are uniform, implying the high flexibility of oxygen sublattices to maintain an overall cubic structure by adjusting their positions. We have also identified the magnetic interaction energies of $A^5\text{Cr}_2\text{O}_4$ are very similar to NiCr_2O_4 due to their similar Cr-O and Cr-Cr bond lengths and A -site spin value.

Unveiling the temperature dependence of $A^5\text{Cr}_2\text{O}_4$'s long-range and local structures presents a compelling avenue for future research as some of the constituent members undergo structural transitions below room temperature [40]. Future investigations into the spin arrangements and potential multiferroic phases are warranted. Furthermore, we believe that our EXAFS analysis approach, which compares CCO with the constituent parent members, can be a powerful tool to reveal subtle details regarding structural modifications in other compositionally complex materials as well. Overall, this study paves the way for a deeper understanding of the impact of local distortions in HEOs, enabling the targeted design of materials with tailored properties.

Methods

Polycrystalline samples of five parent compounds $A\text{Cr}_2\text{O}_4$ ($A = \text{Mn}, \text{Co}, \text{Ni}, \text{Cu}$ and Zn) were synthesized by conventional solid-state synthesis with a stoichiometric amount of Cr_2O_3 and AO . The first heating was carried out at 900°C , followed by a second heat treatment at 1300°C with intermediate grindings. The annealing of MnCr_2O_4 and CuCr_2O_4 were performed in argon and oxygen atmosphere, respectively, while the rest of the compounds were heated in air. The $A^5\text{Cr}_2\text{O}_4$ was synthesized in a similar route in the air. The sample purity of all samples was checked by powder XRD using a laboratory-based Rigaku Smartlab diffractometer. The final XRD patterns were further refined by the Rietveld method using the FULLPROF suite [61]. The temperature-dependent magnetization measurement was carried out in the range of 5 K to 400 K using a commercial SQUID-VSM MPMS from M/s Quantum Design, USA. XAS spectra for $L_{3,2}$ edges of Cr, Mn, Co, Ni, Cu of the $A^5\text{Cr}_2\text{O}_4$ were recorded in total electron yield mode at the beamline 4.0.2 of the Advanced Light Source, USA. Ni $L_{3,2}$ edge of NiCr_2O_4 and Cu $L_{3,2}$ edge of CuCr_2O_4 were also measured.

EXAFS measurements for all transition metal K -edge for all five parent compounds and

$A^{5}\text{Cr}_2\text{O}_4$ have been performed at the P65 beamline, PETRA III Synchrotron Source (DESY, Hamburg, Germany) and at the 20 BM beamline of the Advanced Photon Source, USA. For EXAFS experiments in transmission geometry, the absorbers were prepared by uniformly coating the powder samples on scotch tape. The incident and the transmitted photon energies were simultaneously recorded using the gas ionization chambers as detectors. At each K -edge, at least three scans were collected to average the statistical noise. The analysis was carried out using well-established procedures in the DEMETER suite [62].

For the EXAFS fittings, the amplitude reduction factor S_0^2 and correction to the edge energy ΔE_0 were derived from the analysis of the corresponding standard metal spectra, and these parameters were kept fixed throughout the analysis. The parameters consisting of correction to the bond length ΔR and mean square variation in bond length σ^2 were varied for each scattering path. For the cubic model, ten and eight independent parameters were used in the fittings of A K -edge and Cr K -edge spectra, respectively. Fourteen independent parameters were used for the tetragonal model to fit both Cr K and A K -edges. In the case of NiCr_2O_4 , the number of independent parameters was similar to the cubic model due to the very weak tetragonal distortion.

For $A^{5}\text{Cr}_2\text{O}_4$, a model describing a normal cubic spinel structure was modified to incorporate a solid solution containing equal amounts of Mn, Co, Ni, Cu and Zn at the tetrahedral site. The coordination numbers were constrained to maintain consistency with the cubic spinel structure. A realistic solution-like distribution was simulated for both tetrahedral and octahedral sites by randomly dividing the concerned coordination shell among the five A cations. Furthermore, the five cations were confined to a specific distance from the absorber, independent of the species. The R factor for every fit was less than 2%, indicating the reliability of the fitting outcomes.

ACKNOWLEDGEMENTS

The authors acknowledge the uses of central facilities of the department of Physics, IISc Bangalore, funded by the FIST program of DST (Department of Science and Technology), India. SM acknowledges funding support from a SERB Core Research grant (Grant No. CRG/2022/001906). RN thanks the Indian Institute of Science for support through Sir C. V. Raman postdoctoral fellowship program. SD and NB acknowledge funding from the Prime Minister's Research Fellowship (PMRF), MoE, Government of India. RN also thanks Prof. K.R.S. Priolkar for commenting on the manuscript. UGC-DAE Consortium for Scientific Research, Kalpakkam Node, Kokilamedu, is ac-

knowledge for providing a SQUID-VSM MPMS facility for conducting magnetic measurements, which is part of this work. Portions of this research were carried out at the light source PETRA III DESY, a member of the Helmholtz Association (HGF). Financial support by the Department of Science & Technology (Government of India) provided within the framework of the India@DESY collaboration is gratefully acknowledged. This research used resources of the Advanced Photon Source, a U.S. Department of Energy Office of Science User Facility operated by Argonne National Laboratory under Contract No. DE-AC02-06CH11357. This research used resources of the Advanced Light Source, which is a Department of Energy Office of Science User Facility under Contract No. DE-AC02-05CH11231.

* Contributed equally; rukmagurudas@iisc.ac.in

† Contributed equally

‡ smiddey@iisc.ac.in

- [1] George, E. P., Raabe, D. & Ritchie, R. O. High-entropy alloys. *Nature reviews materials* **4**, 515–534 (2019).
- [2] Sarkar, A. *et al.* High-entropy oxides: fundamental aspects and electrochemical properties. *Advanced materials* **31**, 1806236 (2019).
- [3] Oses, C., Toher, C. & Curtarolo, S. High-entropy ceramics. *Nature Reviews Materials* **5**, 295–309 (2020).
- [4] Musicó, B. L. *et al.* The emergent field of high entropy oxides: Design, prospects, challenges, and opportunities for tailoring material properties. *APL Materials* **8**, 040912 (2020). URL <https://doi.org/10.1063/5.0003149>. https://pubs.aip.org/aip/apm/article-pdf/doi/10.1063/5.0003149/14563544/040912_1_online.pdf.
- [5] Brahlek, M. *et al.* What is in a name: Defining “high entropy” oxides. *APL Materials* **10**, 110902 (2022). URL <https://doi.org/10.1063/5.0122727>. https://pubs.aip.org/aip/apm/article-pdf/doi/10.1063/5.0122727/16490715/110902_1_online.pdf.
- [6] Kotsonis, G. N. *et al.* High-entropy oxides: Harnessing crystalline disorder for emergent functionality. *Journal of the American Ceramic Society* **106**, 5587–5611 (2023).
- [7] Mazza, A. *et al.* Embracing disorder in quantum materials design. *arXiv preprint arXiv:2402.18379* (2024).

- [8] Cantor, B., Chang, I., Knight, P. & Vincent, A. Microstructural development in equiatomic multicomponent alloys. *Materials Science and Engineering: A* **375**, 213–218 (2004).
- [9] Yeh, J.-W. *et al.* Nanostructured high-entropy alloys with multiple principal elements: novel alloy design concepts and outcomes. *Advanced engineering materials* **6**, 299–303 (2004).
- [10] Rost, C. M. *et al.* Entropy-stabilized oxides. *Nature communications* **6**, 8485 (2015).
- [11] Djenadic, R. *et al.* Multicomponent equiatomic rare earth oxides. *Materials Research Letters* **5**, 102–109 (2017).
- [12] Jiang, S. *et al.* A new class of high-entropy perovskite oxides. *Scripta Materialia* **142**, 116–120 (2018).
- [13] Sharma, Y. *et al.* Single-crystal high entropy perovskite oxide epitaxial films. *Physical Review Materials* **2**, 060404 (2018).
- [14] Patel, R. K. *et al.* Epitaxial stabilization of ultra thin films of high entropy perovskite. *Applied Physics Letters* **116**, 071601 (2020).
- [15] Brahlek, M. *et al.* Unexpected crystalline homogeneity from the disordered bond network in $\text{La}(\text{Cr}_{0.2}\text{Mn}_{0.2}\text{Fe}_{0.2}\text{Co}_{0.2}\text{Ni}_{0.2})\text{O}_3$ films. *Phys. Rev. Mater.* **4**, 054407 (2020). URL <https://link.aps.org/doi/10.1103/PhysRevMaterials.4.054407>.
- [16] Musicó, B. *et al.* Tunable magnetic ordering through cation selection in entropic spinel oxides. *Phys. Rev. Mater.* **3**, 104416 (2019). URL <https://link.aps.org/doi/10.1103/PhysRevMaterials.3.104416>.
- [17] Sharma, Y. *et al.* Magnetic texture in insulating single crystal high entropy oxide spinel films. *ACS applied materials & interfaces* **13**, 17971–17977 (2021).
- [18] Johnstone, G. H. *et al.* Entropy engineering and tunable magnetic order in the spinel high-entropy oxide. *Journal of the American Chemical Society* **144**, 20590–20600 (2022).
- [19] Wright, A. J. *et al.* Size disorder as a descriptor for predicting reduced thermal conductivity in medium-and high-entropy pyrochlore oxides. *Scripta Materialia* **181**, 76–81 (2020).
- [20] Jiang, B. *et al.* Probing the local site disorder and distortion in pyrochlore high-entropy oxides. *Journal of the American Chemical Society* **143**, 4193–4204 (2020).
- [21] Kinsler-Fedon, C. *et al.* Synthesis, characterization, and single-crystal growth of a high-entropy rare-earth pyrochlore oxide. *Phys. Rev. Mater.* **4**, 104411 (2020). URL <https://link.aps.org/doi/10.1103/PhysRevMaterials.4.104411>.

- [22] Sarkar, A. *et al.* High entropy oxides for reversible energy storage. *Nature communications* **9**, 3400 (2018).
- [23] Chen, H. *et al.* Entropy-stabilized metal oxide solid solutions as co oxidation catalysts with high-temperature stability. *Journal of Materials Chemistry A* **6**, 11129–11133 (2018).
- [24] Braun, J. L. *et al.* Charge-induced disorder controls the thermal conductivity of entropy-stabilized oxides. *Advanced materials* **30**, 1805004 (2018).
- [25] Kante, M. V. *et al.* A high entropy oxide as high-activity electrocatalyst for water oxidation. *ACS Nano* **17**, 5329 (2023). URL <https://pubs.acs.org/doi/10.1021/acsnano.2c08096>.
- [26] Patel, R. K. *et al.* Thickness dependent OER electrocatalysis of epitaxial thin film of high entropy oxide. *Applied Physics Reviews* **10**, 031407 (2023). URL <https://doi.org/10.1063/5.0146005>. https://pubs.aip.org/aip/apr/article-pdf/doi/10.1063/5.0146005/18068792/031407_1_5.0146005.pdf.
- [27] Zhao, B. *et al.* High-entropy enhanced microwave attenuation in titanate perovskites. *Advanced Materials* **35**, 2210243 (2023).
- [28] Schweidler, S. *et al.* High-entropy materials for energy and electronic applications. *Nature Reviews Materials* 1–16 (2024).
- [29] Aamlid, S. S., Oudah, M., Rottler, J. & Hallas, A. M. Understanding the role of entropy in high entropy oxides. *Journal of the American Chemical Society* **145**, 5991–6006 (2023).
- [30] Ruffoni, M., Pettifer, R., Pascarelli, S., Trapananti, A. & Mathon, O. Probing atomic displacements with thermal differential exafs. *Journal of Synchrotron Radiation* **14**, 421–425 (2007).
- [31] Newville, M. Fundamentals of xafs. *Reviews in Mineralogy and Geochemistry* **78**, 33–74 (2014).
- [32] Rehr, J. J. & Albers, R. C. Theoretical approaches to x-ray absorption fine structure. *Rev. Mod. Phys.* **72**, 621–654 (2000). URL <https://link.aps.org/doi/10.1103/RevModPhys.72.621>.
- [33] Rost, C. M., Rak, Z., Brenner, D. W. & Maria, J.-P. *Journal of the American Ceramic Society* **100**, 2732–2738 (2017).
- [34] Pu, Y. *et al.* (mg, mn, fe, co, ni) o: A rocksalt high-entropy oxide containing divalent mn and fe. *Science Advances* **9**, eadi8809 (2023).
- [35] Tsurkan, V., Von Nidda, H.-A. K., Deisenhofer, J., Lunkenheimer, P. & Loidl, A. On the complexity of spinels: Magnetic, electronic, and polar ground states. *Physics Reports* **926**, 1–86 (2021).

- [36] Tomiyasu, K., Fukunaga, J. & Suzuki, H. Magnetic short-range order and reentrant-spin-glass-like behavior in CoCr_2O_4 and MnCr_2O_4 by means of neutron scattering and magnetization measurements. *Physical Review B* **70**, 214434 (2004).
- [37] Bhowmik, R., Ranganathan, R. & Nagarajan, R. Lattice expansion and noncollinear to collinear ferrimagnetic order in a MnCr_2O_4 nanoparticle. *Physical Review B* **73**, 144413 (2006).
- [38] Yamasaki, Y. *et al.* Magnetic reversal of the ferroelectric polarization in a multiferroic spinel oxide. *Physical review letters* **96**, 207204 (2006).
- [39] Dey, K., Majumdar, S. & Giri, S. Ferroelectricity in spiral short-range-ordered magnetic state of spinel MnCr_2O_4 : Significance of topological frustration and magnetoelastic coupling. *Physical Review B* **90**, 184424 (2014).
- [40] Suchomel, M. R., Shoemaker, D. P., Ribaud, L., Kemei, M. C. & Seshadri, R. Spin-induced symmetry breaking in orbitally ordered NiCr_2O_4 and CuCr_2O_4 . *Physical Review B* **86**, 054406 (2012).
- [41] Dutton, S. E., Huang, Q., Tchernyshyov, O., Broholm, C. & Cava, R. J. Sensitivity of the magnetic properties of the ZnCr_2O_4 and MgCr_2O_4 spinels to nonstoichiometry. *Physical Review B* **83**, 064407 (2011).
- [42] Van Der Laan, G., Chopdekar, R., Suzuki, Y. & Arenholz, E. Strain-induced changes in the electronic structure of MnCr_2O_4 thin films probed by x-ray magnetic circular dichroism. *Physical review letters* **105**, 067405 (2010).
- [43] Kim, I. *et al.* Electric polarization enhancement in multiferroic CoCr_2O_4 crystals with Cr-site mixing. *Applied Physics Letters* **94** (2009).
- [44] Shannon, R. t. & Prewitt, C. Revised values of effective ionic radii. *Acta Crystallographica Section B: Structural Crystallography and Crystal Chemistry* **26**, 1046–1048 (1970).
- [45] Stöhr, J. & Siegmann, H. C. Magnetism. *Solid-State Sciences. Springer, Berlin, Heidelberg* **5**, 236 (2006).
- [46] Windsor, Y. W. *et al.* Magnetic properties of strained multiferroic CoCr_2O_4 : A soft x-ray study. *Physical Review B* **95**, 224413 (2017).
- [47] Rák, Z., Maria, J.-P. & Brenner, D. Evidence for Jahn-Teller compression in the (Mg, Co, Ni, Cu, Zn) O entropy-stabilized oxide: A DFT study. *Materials Letters* **217**, 300–303 (2018).
- [48] Kaplan, T. & Menyuk, N. Spin ordering in three-dimensional crystals with strong competing exchange interactions. *Philosophical Magazine* **87**, 3711–3785 (2007).

- [49] Kaplan, T. A. Classical theory of spin configurations in the cubic spinel. *Phys. Rev.* **119**, 1460–1470 (1960). URL <https://link.aps.org/doi/10.1103/PhysRev.119.1460>.
- [50] Winkler, E. *et al.* Magnetocrystalline interactions in MnCr_2O_4 spinel. *Physical Review B* **80**, 104418 (2009).
- [51] Ederer, C. & Komelj, M. Magnetic coupling in CoCr_2O_4 and MnCr_2O_4 : An LSDA + U study. *Phys. Rev. B* **76**, 064409 (2007). URL <https://link.aps.org/doi/10.1103/PhysRevB.76.064409>.
- [52] Witte, R. *et al.* High-entropy oxides: An emerging prospect for magnetic rare-earth transition metal perovskites. *Phys. Rev. Mater.* **3**, 034406 (2019). URL <https://link.aps.org/doi/10.1103/PhysRevMaterials.3.034406>.
- [53] Sharma, Y. *et al.* Magnetic anisotropy in single-crystal high-entropy perovskite oxide $\text{La}(\text{Cr}_{0.2}\text{Mn}_{0.2}\text{Fe}_{0.2}\text{Co}_{0.2}\text{Ni}_{0.2})\text{O}_3$ films. *Phys. Rev. Mater.* **4**, 014404 (2020). URL <https://link.aps.org/doi/10.1103/PhysRevMaterials.4.014404>.
- [54] Mazza, A. R. *et al.* Charge doping effects on magnetic properties of single-crystal $\text{La}_{1-x}\text{Sr}_x(\text{Cr}_{0.2}\text{Mn}_{0.2}\text{Fe}_{0.2}\text{Co}_{0.2}\text{Ni}_{0.2})\text{O}_3$ ($0 \leq x \leq 0.5$) high-entropy perovskite oxides. *Phys. Rev. B* **104**, 094204 (2021). URL <https://link.aps.org/doi/10.1103/PhysRevB.104.094204>.
- [55] Mazza, A. R. *et al.* Designing magnetism in high entropy oxides. *Advanced Science* **9**, 2200391 (2022).
- [56] Su, L. *et al.* Direct observation of elemental fluctuation and oxygen octahedral distortion-dependent charge distribution in high entropy oxides. *Nature communications* **13**, 2358 (2022).
- [57] Mugiraneza, S. & Hallas, A. M. Tutorial: a beginner’s guide to interpreting magnetic susceptibility data with the curie-weiss law. *Communications Physics* **5**, 95 (2022).
- [58] Coey, J. M. D. *Magnetism And Magnetic Materials* (Cambridge University Press, U.K., 2010).
- [59] Kassem, M. A., El-Fadl, A. A., Nashaat, A. M. & Nakamura, H. Structural, optical and single-domain magnetic features of the noncollinear ferrimagnetic nano-spinel chromites ACr_2O_4 (A= Ni, Co, and Mn). *arXiv preprint arXiv:2305.17856* (2023).
- [60] Lee, S.-H., Broholm, C., Kim, T., W Ratcliff, I. & Cheong, S.-W. Local spin resonance and spin-peierls-like phase transition in a geometrically frustrated antiferromagnet. *Physical Review Letters* **84**, 3718 (2000).

- [61] J.Rodríguez-Carvajal. Recent developments of the program fullprof, in commission on powder diffraction (iucr). *Newsletter* **26**, 12–19 (2001).
- [62] Ravel, B. & Newville, M. Athena, artemis, hephaestus: data analysis for x-ray absorption spectroscopy using ifeffit. *Journal of synchrotron radiation* **12**, 537–541 (2005).